PHYSICAL REVIEW FLUIDS **7**, 084504 (2022)

Hydrodynamic slip significantly alters chaotic advection and scattering of small particles

Jason K. Kabarowski and Aditya S. Khair[*]
Department of Chemical Engineering, Carnegie Mellon University, Pittsburgh, Pennsylvania 15213, USA

(Received 26 January 2022; accepted 9 August 2022; published 31 August 2022)

The motion of small spherical particles in unsteady fluid flow can be predicted using the Boussinesq-Basset-Oseen equation, which is an integrodifferential equation balancing the particle inertia with the unsteady hydrodynamic force on a particle. For rigid spherical particles on whose surface the no-slip condition is obeyed, the Basset history force has been shown to significantly alter the statistical behavior of ensembles of particles in unsteady flows [Daitche and Tél, Phys. Rev. Lett. **107**, 244501 (2011)]. Here, we determine the effect of hydrodynamic slip at the surface of the particle on the statistical behavior of an ensemble of spherical particles in a two-dimensional von Kármán flow in the wake of a cylinder. We compute the dynamics of a large quantity of spherical particles (on the order of a million) in this flow, and therefrom calculate escape rates, invariant manifold locations, and the uncertainty dimension of scattering trajectories for two cases: no-slip spheres and perfectly slipping spheres. We compare individual particle trajectories, locations of invariant manifolds, and residence time distributions for the two cases. We find that the presence of slip on a particle can lead to significant differences in escape rates, more initial positions that lead to vortex trapping at long times, and a greater uncertainty in scattering predictions. Thus, our paper shows that hydrodynamic slip significantly affects particle trajectories in unsteady flows.

DOI: 10.1103/PhysRevFluids.7.084504

I. INTRODUCTION

The motion of small inertial particles in an unsteady fluid flow is relevant to cloud microphysics [1], particle clustering in turbulence [2,3], bubbles in sound waves [4], micro-organism movement [5], and pollutant transport [6]. Such particles often move in a viscous fluid at a small particle-scale Reynolds number, $\mathrm{Re}_p = aW/\nu \ll 1$, where a is the characteristic size of the particle (e.g., the radius for a spherical object), ν is the kinematic viscosity of the fluid, and $W = |\boldsymbol{v} - \boldsymbol{u}|$ is a characteristic relative speed with particle velocity, $\boldsymbol{v}$, and local fluid velocity, $\boldsymbol{u}$ [7]. Although Re_p is small, unsteadiness from a time-dependent ambient flow and the disturbance flow induced by the particle leads to inertial effects when $\mathrm{Re}_p\mathrm{Sl} = (a^2/\nu)/\tau = O(1)$, where $\mathrm{Sl} = a/(W\tau)$ is the Strouhal number and τ is a timescale that characterizes the unsteadiness of the ambient flow. That is, unsteady effects can be important when the momentum diffusion timescale across the particle, $\tau_\nu = a^2/\nu$, is on the order of the unsteadiness timescale in the flow. For example, τ_ν is around one second for a sphere with radius of 1 mm in water. In this regime, the hydrodynamic force, $\boldsymbol{F}_{\mathrm{NS}}$, due to the disturbance flow around a spherical particle on whose surface the no-slip boundary condition

---

[*] akhair@andrew.cmu.edu

is obeyed is given by [8]

$$\boldsymbol{F}_{\mathrm{NS}} = -\frac{m_f}{2}\left(\frac{d\boldsymbol{v}}{dt} - \frac{d\boldsymbol{u}}{dt}\right) - 6\pi a\rho_f\nu(\boldsymbol{v}-\boldsymbol{u}) - 6a^2\rho_f\sqrt{\pi\nu}\frac{d}{dt}\int_{t_0}^{t} K(t-s)(\boldsymbol{v}(s)-\boldsymbol{u}(s))ds, \quad (1)$$

where the memory kernel

$$K(t) = \begin{cases} \frac{1}{\sqrt{t}} & \text{for } t \geqslant 0 \\ 0 & \text{for } t < 0. \end{cases} \quad (2)$$

Here, m_p is the mass of the particle, m_f is the mass of the fluid displaced by the particle, ρ_f is the fluid density, and

$$\frac{d\boldsymbol{u}}{dt} = \frac{\partial\boldsymbol{u}}{\partial t} + \boldsymbol{v}\cdot\nabla\boldsymbol{u} \quad (3)$$

and

$$\frac{d\boldsymbol{u}}{dt} = \frac{\partial\boldsymbol{u}}{\partial t} + \boldsymbol{u}\cdot\nabla\boldsymbol{u} \quad (4)$$

are the material derivatives along a particle path line and fluid streamline, respectively. The acceleration reaction, which is the first term on the right of Eq, (1), is the force on the particle due to an inviscid pressure disturbance caused by the changing velocity of the particle. The Stokes drag, the second term on the right, is the instantaneous force on the particle due to viscous effects. The Basset force, the third term on the right, is a memory integral that relates the force on the particle at the current time, t, to the past history of the particle velocity from an initial time, t_0, and originates from the unsteady diffusion of vorticity [9].

Hydrodynamic slip at the particle surface alters the hydrodynamic force on a particle. The force on a perfectly slipping spherical particle (that is, where the particle surface cannot support a shear stress) is [10,11]

$$\boldsymbol{F}_S = -\frac{m_f}{2}\left(\frac{d\boldsymbol{v}}{dt} - \frac{d\boldsymbol{u}}{dt}\right) - 4\pi a\rho_f\nu(\boldsymbol{v}-\boldsymbol{u}) - 8\pi a\rho_f\nu\frac{d}{dt}\int_{t_0}^{t} G(t-s)(\boldsymbol{v}(s)-\boldsymbol{u}(s))ds, \quad (5)$$

where the kernel

$$G(t) = \begin{cases} \mathrm{e}^{9t\nu/a^2}\operatorname{erfc}(\sqrt{9t\nu/a^2}) & \text{for } t \geqslant 0 \\ 0 & \text{for } t < 0, \end{cases} \quad (6)$$

and erfc$(\cdot)$ is the complementary error function. The introduction of hydrodynamic slip nontrivially alters the force. Specifically, while the Stokes drag is simply two-thirds the magnitude of the no-slip case and the acceleration reaction is unchanged, the memory kernel, $G(t)$, has taken a new functional form. This new memory kernel for a perfectly slipping sphere is bounded as $t \to 0$, whereas the no-slip memory kernel, $K(t)$, is (integrably) singular as $t \to 0$. As $t \to \infty$, both memory kernels decay algebraically as $t^{-1/2}$. This algebraic decay has important implications; for instance, it leads to a long-time tail in the velocity autocorrelation function of a particle undergoing Brownian motion [12].

The memory kernel $K(t)$ only applies to rigid spherical particles on whose surface the no-slip condition is satisfied. That is, Premlata and Wei [13] showed that the memory kernel for a rigid sphere with any nonzero slip length will maintain the same functional form as Eq. (6); however, the characteristic momentum diffusion time is now a function of the ratio of the slip length to particle radius. Kabarowski and Khair [14] calculated the time-dependent velocity of a perfectly slipping sphere and showed that the high frequency, or short time, dynamics are most sensitive to slip. Indeed, Mo *et al.* [15] suggested that measurement of the short-time Brownian motion of single spheres could be used to infer slip length. Galindo and Gerbeth [16] derived the equivalent memory kernel for a spherical viscous drop in the Fourier time domain, which, in the large drop viscosity to fluid viscosity ratio limit, exhibits the behavior of the no-slip memory kernel, $K(t)$, and in the inviscid bubble limit, a perfect slip memory kernel, $G(t)$. This is unlike a rigid sphere with finite slip that, as mentioned above, has a memory kernel of the same functional form as the perfect slip memory kernel. We emphasize, then, that Eq. (1) pertains only to a rigid, no-slip spherical particle; for a drop, bubble, partially or perfectly slipping sphere, there is a different kernel associated with the unsteady force on the particle. While the works described above have shown how this difference in the unsteady force affects the motion of a single particle, analysis of the collective motion of many particles is lacking. It is the purpose of the present paper to address this gap in knowledge, for the specific case of perfectly slipping spheres.

Ensemble dynamics of many particles at low Reynolds number are important in chaotic advection, where a laminar flow exhibits chaos, thereby enhancing mixing [17]. This effect has been exploited in microfluidics, where a microchannel is constructed into a square wave to promote mixing [18]. Open flow chaotic systems, such as flows in the wake of obstacles, are of interest in continuous flow reactor modeling [19]. For no-slip spheres in open chaotic flows, the Basset force has been shown to significantly influence the statistical behavior of ensembles of particles that remain in the wake of the cylinder for times on the order of ten vortex shedding periods or larger [8]. Not only do particle trajectories deviate due to inclusion of the Basset force, which is expected due to the sensitivity to initial conditions, but also the statistical properties of an ensemble of particles including escape rates, location of attractors, and residence time distributions. A natural question to ask, then, is how such statistical properties are affected by the difference in unsteady force on a particle owing to hydrodynamic slip.

In this paper, we show that hydrodynamic slip significantly alters the statistical behavior of spherical particles in an open chaotic flow. We compute the trajectories of perfectly slipping spheres advected in the two-dimensional wake of a cylinder. We calculate collective behavior of the particles to provide a statistical representation of their dynamics and compare to no-slip spheres and fluid elements (i.e., passive tracers). We demonstrate that the presence of slip increases escape rates for particles more dense than the surrounding fluid and decreases escape rates for particles less dense than the surrounding fluid. Using residence time distributions, it is shown that the time that a particle remains trapped in the wake of the cylinder can be orders of magnitude different between slip and no-slip spheres given the same initial condition. We calculate the finite time Lyapunov exponent (FTLE) field to trace the unstable (attracting) manifold and the stable (repelling) manifold to compare the unsteady dynamics of a no-slip and slip particle. In Sec. II, we provide a problem formulation along with a description of the method used for trajectory computation. In Sec. III, we compare the differences of no-slip and slipping spheres in chaotic advection. In Sec. IV, we compute chaotic scattering behavior for no-slip and slipping spheres. In Sec. V, a conclusion is offered.

II. PROBLEM FORMULATION

The motion of a small rigid sphere to which fluid perfectly adheres (i.e., the no-slip condition is obeyed) in an unsteady flow is governed by the Basset-Boussinesq-Oseen (BBO) equation [9]:

$$m_p \frac{d\boldsymbol{v}}{dt} = m_f \frac{d\boldsymbol{u}}{dt} + \boldsymbol{F}_{\mathrm{NS}}. \tag{7}$$

The left-hand side of Eq. (7) is the particle inertia. The first term on the right-hand side is the hydrodynamic force from the undisturbed flow, which is sometimes referred to as the pressure gradient term. This term originates from the acceleration of the undisturbed flow and is the only hydrodynamic force component acting on a fluid element. The second term on the right-hand side is the hydrodynamic force due to the disturbance flow generated by the particle. Here, we take $\boldsymbol{F}_{\mathrm{NS}}$ to be given by Eq. (1), which is contingent on the disturbance flow at the particle scale obeying the unsteady Stokes equations. As discussed by Maxey and Riley (MR) [7], this requires $\mathrm{Re}_s \ll 1$, $\mathrm{Re}_p = aW/\nu \ll 1$, and $\mathrm{Re}_p Sl = (a^2/\tau\nu) = O(1)$. Here, $\mathrm{Re}_s = (a^2 s/\nu)$ is a shear Reynolds number, where $s = U/L$ is the characteristic shear rate of the undisturbed flow, in which L is the length scale of the undisturbed flow and U is the characteristic magnitude of the undisturbed velocity field $\boldsymbol{u}$. Additionally, we do not consider Faxen's corrections to $\boldsymbol{F}_{\mathrm{NS}}$, arising from spatial variations in the undisturbed flow, which requires $a/L \ll 1$. If such corrections were included, then Eq. (7) would be termed the MR equation [7,20], rather than the BBO equation. Buoyancy effects are also omitted, which is valid in the present two-dimensional flow scenario. Inclusion of the Basset force makes Eq. (7) an integrodifferential equation.

We now substitute Eq. (1) into Eq. (7) and introduce a characteristic unsteadiness time scale, τ, characteristic length scale, a, and thereby nondimensionalize Eq. (7), yielding

$$\frac{d\boldsymbol{v}}{dt} = \gamma\frac{d\boldsymbol{u}}{dt} - \frac{3\gamma}{\mathrm{Re}_p\mathrm{Sl}}(\boldsymbol{v}-\boldsymbol{u}) - 3\gamma\sqrt{\frac{1}{\pi}\frac{1}{\mathrm{Re}_p Sl}}\frac{d}{dt}\int_{t_0}^{t} K(t-s)(\boldsymbol{v}(s)-\boldsymbol{u}(s))ds, \tag{8}$$

where $K(t-s) = 1/\sqrt{t-s}$, and

$$\gamma = \frac{3m_f}{m_f + 2m_p} \tag{9}$$

is the dimensionless density ratio with an inviscid bubble pertaining to $\gamma = 3$, a neutrally buoyant particle as $\gamma = 1$, and particles more dense than the fluid have $\gamma < 1$. The dimensionless group in Eq. (8) is

$$\mathrm{Re}_p\mathrm{Sl} = \frac{a^2/\nu}{\tau}, \tag{10}$$

which represents the ratio of the momentum diffusion time and the unsteadiness time.

In contrast, the equation of motion of a perfectly slipping spherical particle is [21]

$$m_p\frac{d\boldsymbol{v}}{dt} = m_f\frac{d\boldsymbol{u}}{dt} + \boldsymbol{F}_S. \tag{11}$$

The dimensionless form of (11) after substitution of (5) is

$$\frac{d\boldsymbol{v}}{dt} = \gamma\frac{d\boldsymbol{u}}{dt} - 2\frac{\gamma}{Re_pSl}(\boldsymbol{v}-\boldsymbol{u}) - 4\frac{\gamma}{Re_pSl}\frac{d}{dt}\int_{t_0}^{t} G(t-s)(\boldsymbol{v}(s)-\boldsymbol{u}(s))ds, \tag{12}$$

where

$$G(t-s) = \mathrm{e}^{9(t-s)/\mathrm{Re}_p\mathrm{Sl}}\mathrm{erfc}(\sqrt{9(t-s)/\mathrm{Re}_p\mathrm{Sl}}). \tag{13}$$

To quantify the effect of slip on the ensemble dynamics of particles, we will compute the trajectories of $O(10^6)$ particles in a chaotic flow. A two-dimensional von Kármán flow in the wake of a cylinder will be adopted, since an analytical approximation is available for the stream function of the flow. Jung *et al.* [19] obtained this stream function, also known as a JTZ flow, and it has been shown to capture the correct qualitative behavior of experiments. Specifically, Sommerer *et al.* [22] performed experiments of a moving cylinder through a cross-streamline stripe of dye and found the initial exponential rate of escape of fluid elements to match that predicted by the JTZ stream function. However, at long times the escape rate did not match with the JTZ-based prediction of an algebraic decay. This could be due to the simplified expression in the JTZ stream function for the fluid boundary layer at the cylinder surface. The JTZ stream function is defined as

$$\psi(x,y,t) = f(x,y)g(x,y,t), \tag{14}$$

where the origin is at the center of the cylinder of unit radius, x is in the direction of the flow, and y is perpendicular to x. Here,

$$f(x,y) = 1 - \exp[-((x^2+y^2)^{1/2}-1)^{1/2}], \tag{15}$$

which describes the boundary layer at the cylinder surface and tends to unity as distance from the cylinder increases. The second factor, $g(x,y,t)$, contains information on the behavior of the two vortices in the wake of the cylinder and is given by

$$g(x, y, t) = -wH_1(t)g_1(x, y, t) + wH_2(t)g_2(x, y, t) + 14ys(x, y), \tag{16}$$

where w is the vortex strength, $H_1(t) = \sin^2(\pi t)$, $H_2 = \cos^2(\pi t)$, and

$$g_1(x, y, t) = \exp[-0.35(x - x_1(t))^2 + 4(y - 0.3)^2], \tag{17}$$

$$g_2(x, y, t) = \exp[-0.35(x - x_2(t))^2 + 4(y - 0.3)^2], \tag{18}$$

where $x_1(t)$ and $x_2(t)$ are the x positions of the vortices that change with time as

$$x_1(t) = 1 + 2\,\mathrm{frac}(t), \tag{19}$$

$$x_2(t) = 1 + 2\,\mathrm{frac}(t - 1/2), \tag{20}$$

where frac(z) is the fractional part/decimal part of z, that is, the excess decimals after the integer. The last term, $s(x, y)$, is given by

$$s(x, y) = 1 - \exp\left(-\tfrac{1}{4}(x - 1)^2 - y^2\right), \tag{21}$$

and describes the flow near the rear of the cylinder as it pertains to vortices being shed. The unsteadiness timescale is taken to be the period of vortex shedding, and the dimensionless vortex strength is selected as $w = 192/\pi$ for our computations. Figure 1 provides two snapshots in time of the flow. In Fig. 1(a), $t = 0.45$, a first vortex has shed from the cylinder surface, and by $t = 0.75$, in Fig. 1(b), a second vortex is being shed from the opposite side of the cylinder.

We compute particle motion in this flow field using a second-order Adams-Bashforth predictor-corrector scheme as well as a second-order Newton-Cotes integration method for $G(t)$ and a-second order method for $K(t)$ described by Daitche [23]. For the no-slip case, we begin by defining $\boldsymbol{w} = \boldsymbol{v} - \boldsymbol{u}$ and rewrite Eq. (8) as

$$\frac{d\boldsymbol{w}}{dt} = (\gamma - 1)\frac{d\boldsymbol{u}}{dt} - \frac{3\gamma}{\mathrm{Re}_p\mathrm{Sl}}\boldsymbol{w} - \gamma\boldsymbol{w}\cdot\nabla\boldsymbol{u} - 3\gamma\sqrt{\frac{1}{\pi}\frac{1}{\mathrm{Re}_p\mathrm{Sl}}}\frac{d}{dt}\int_{t_0}^{t} K(t - s)\boldsymbol{w}ds. \tag{22}$$

The position of a particle evolves according to

$$\frac{d\boldsymbol{r}}{dt} = \boldsymbol{v} = \boldsymbol{w} + \boldsymbol{u}, \tag{23}$$

where $\boldsymbol{r}$ is the position vector of the particle relative to the origin at the center of the cylinder. We now split Eq. (22) into two parts, A and B, namely,

$$A = (\gamma - 1)\frac{d\boldsymbol{u}}{dt} - \frac{3\gamma}{\mathrm{Re}_p\mathrm{Sl}}\boldsymbol{w} - \gamma\boldsymbol{w}\cdot\nabla\boldsymbol{u}, \tag{24}$$

$$B = -3\gamma\sqrt{\frac{1}{\pi}\frac{1}{\mathrm{Re}_p\mathrm{Sl}}}\frac{d}{dt}\int_{t_0}^{t} K(t - s)\boldsymbol{w}ds, \tag{25}$$

where B contains the history integral, which is calculated to second order using the coefficients β_j^n defined on p. 6 of Ref. [23]. The time-stepping scheme for particle position at time $t_{n+1} = t_n + h$, where h is the step size, is

$$\boldsymbol{r}(t_{n+1}) = \boldsymbol{r}(t_n) + \frac{h}{2}[3(\boldsymbol{w}(t_n) + \boldsymbol{u}(t_n)) - (\boldsymbol{w}(t_{n-1}) + \boldsymbol{u}(t_{n-1}))], \tag{26}$$

and relative velocity is stepped according to

$$\left(1 + \zeta\beta_0^{n+1}\right)\boldsymbol{w}(t_{n+1}) = \boldsymbol{w}(t_n) + \frac{h}{2}(3A(t_n) - A(t_{n-1})) - \zeta\,\Sigma_{j=0}^{n}\left(\beta_{j+1}^{n+1}\boldsymbol{w}(t_{n-j}) - \beta_j^n\boldsymbol{w}(t_{n-j})\right), \tag{27}$$

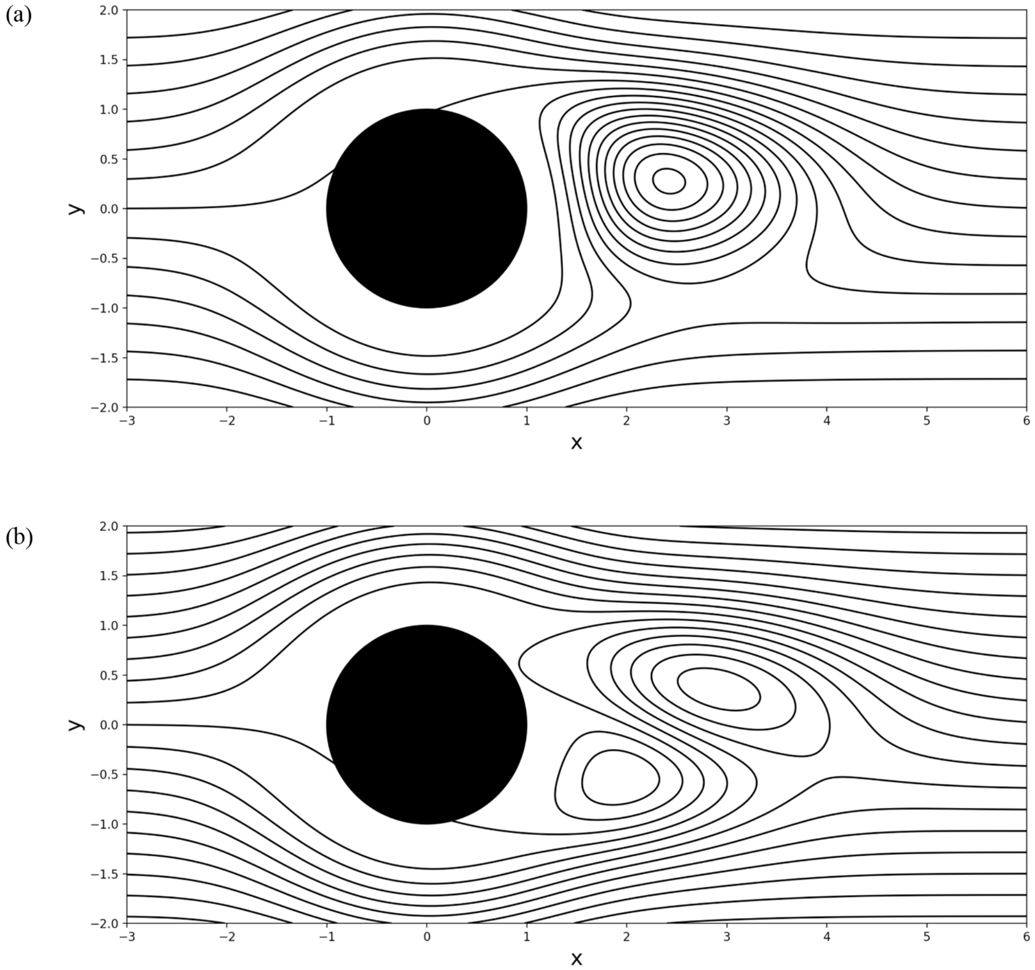

FIG. 1. Streamline plot of the JTZ flow in the wake of a cylinder with streamlines in increments of 3 of the stream function. Snapshots are taken at (a) $t = 0.45$ and (b) $t = 0.75$, illustrating the shedding of vortices from the cylinder surface. The single vortex shed in (a) is squashed by the second vortex shed in (b).

where $\zeta = 3\gamma\sqrt{h/(\pi \mathrm{Re}_p \mathrm{Sl})}$. The second-order method has been shown to be accurate for long computation times [$O(10^4)$ time steps] with a time step $h = 0.01$ (see Fig. 3 in Ref. [23]). This method allows for accurate trajectory computation given the integrably singular no-slip memory kernel $K(t)$. In contrast, the perfect slip memory kernel $G(t)$ is finite as $t \to 0$ and trajectories can be computed accurately in this case with simpler methods such as the second-order Newton-Cotes scheme.

III. CHAOTIC ADVECTION

A. Individual trajectories and escape rates

We first calculate the trajectories of both a no-slip sphere and perfectly slipping sphere (Fig. 2). Here, we compute starting from the same upstream initial position ($x = -1$, $y = -1.2$), density ratio $\gamma = 0.6$, and initial time $t_0 = 0.2$; however, the hydrodynamic forces acting on these spheres are different due to the presence/absence of slip. The initial time was chosen to match the no-slip trajectory computed by Daitche and Tél [24], and our computation of this trajectory

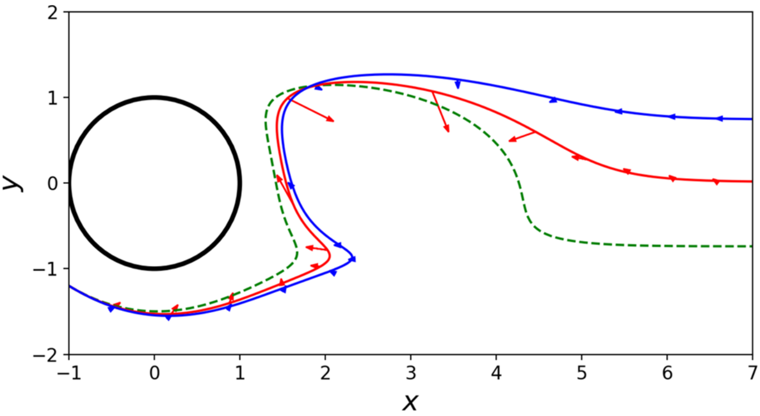

FIG. 2. Trajectories of a no-slip sphere and perfectly slipping sphere from the initial position $(-1, -1.2)$, density ratio $\gamma = 0.6$, and initial time $t_0 = 0.2$, where red: no-slip, blue: perfect slip, and green: fluid element. Arrows indicated the magnitude and direction of the history force for each case: the magnitude of the history force is smaller in the perfect slip case throughout the entire trajectory.

compares favorably to theirs. We observe that the trajectories of the perfectly slipping sphere and no-slip sphere deviate downstream: at $x \approx 7$, they are almost one cylinder radius apart. This difference is due to the cumulative effect of small differences in the instantaneous force acting on the particle, adding up to produce a large effect downstream. As the path lines of the particles begin to diverge, the history of the particle velocity changes. Thus, not only is the memory kernel weighting past velocity differently, the past velocities can also significantly differ.

Statistics of ensemble dynamics are needed to further describe the differences between the slip and no-slip cases. In Fig. 3(b), we compute $N = 1.6 \times 10^6$ particles in the wake of the cylinder for $\gamma = 0.6$ and $\mathrm{Re}_p\mathrm{Sl} = 0.09$ over the interval $x = (0.6, 4)$ and $y = (-2, 2)$ and calculate the rate at which no-slip and slipping spheres escape. An escaped particle is defined as a particle that passes $x = 5$ or moves within 0.014 radii of the cylinder surface. The second condition is used to only include particles which escape downstream at intermediate times where the number of unescaped particles, $N(t)$, decays exponentially as shown in Fig. 3(b). The number of unescaped particles at longer times decay according to a power law or may get stuck on the cylinder surface and never escape [19]. We define an escape rate through $N(t) \sim \exp(-\kappa t)$, where κ is the escape rate. The computation in Fig. 3(b) yields $\kappa = 1.08$ for a no-slip sphere and $\kappa = 1.32$ for a perfectly slipping sphere. The inverse of escape rate is the average chaotic lifetime of a particle. That is, a particle with

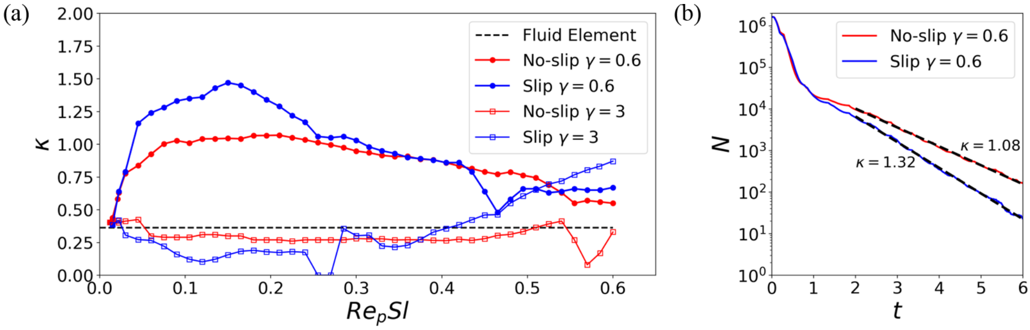

FIG. 3. (a) Escape rates of a no-slip sphere and a perfectly slipping sphere during intermediate times between $t = 3$ and $t = 25$ of the flow versus $\mathrm{Re}_p\mathrm{Sl}$ and (b) the number of unescaped particles $N(t)$ versus t for a computation for no-slip and perfectly slipping spheres at $\mathrm{Re}_p\mathrm{Sl} = 0.09$ and $\gamma = 0.6$.

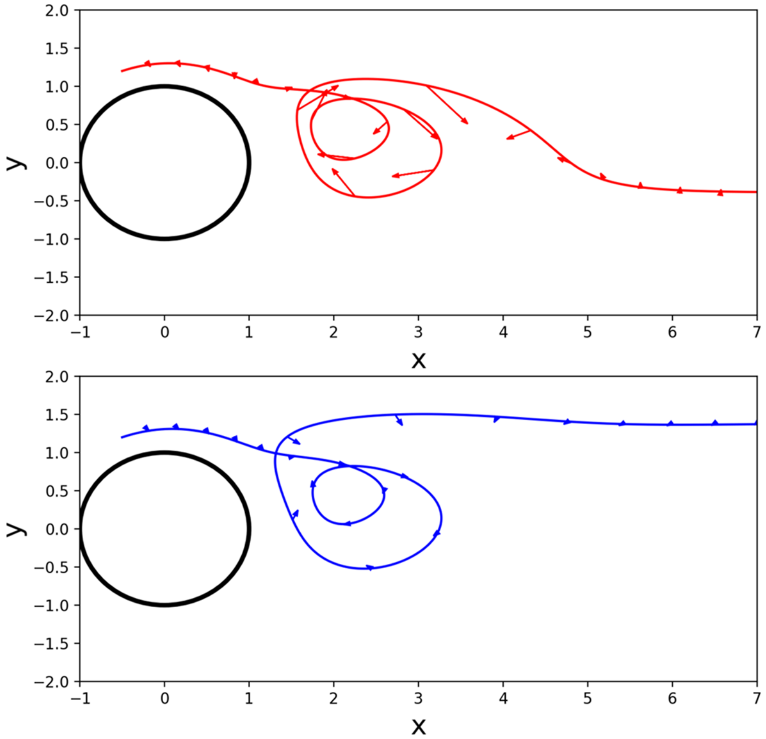

FIG. 4. Comparison of trajectories of a no-slip sphere (top, red) versus perfectly slipping sphere (bottom, blue). Initial particle positions are (−.5, 1.2), $\mathrm{Re}_p\mathrm{Sl} = 0.045$, $t_0 = 0$ and $\gamma = 0.6$. The arrows indicate the direction and magnitude of the history force along the trajectory: the magnitude of the history force is smaller in the perfect slip case throughout the entire trajectory.

a slow escape rate (small κ) remains in the chaotic wake of the cylinder longer than a particle with a fast escape rate (large κ).

In Fig. 3(a), our results for the escape rate of fluid elements and no-slip spheres match that of Daitche and Tél [8] for $\mathrm{Re}_p\mathrm{Sl} < 0.3$, with 0.3 being the largest value they studied: note, our computation range extends to $\mathrm{Re}_p\mathrm{Sl} = 0.6$. We observe that for all particles, as $\mathrm{Re}_{\mathrm{pSl}} \to 0$, the escape rates approach the escape rate of a fluid element, which makes sense as memory effects should be negligible in this limit. However, at different $\mathrm{Re}_p\mathrm{Sl}$, the escape rate for a no-slip versus perfect slip particle can vary significantly. For $0.05 < \mathrm{Re}_p\mathrm{Sl} < 0.2$ and $\gamma = 0.6$, the escape rate can differ by over 50% due to the presence of slip, with the slipping spheres having a larger escape rate. Thus, the exponential sensitivity of $N(t)$ on escape rate leads to two-thirds more time needed for half of the particles to escape in the no-slip case than the perfect slip case. For $0.3 < \mathrm{Re}_p\mathrm{Sl} < 0.5$ and $\gamma = 0.6$, the escape rates are similar. As we increase $\mathrm{Re}_p\mathrm{Sl}$, it is difficult to predict *a priori* whether a no-slip or perfect slip sphere will escape more quickly, due to the chaotic nature of particle trajectories within the wake flow. For instance, for particles of $\gamma = 3$ and $\mathrm{Re}_p\mathrm{Sl} < 0.25$, the escape rate of the perfectly slipping sphere is lower than that of a no-slip sphere. In addition, we found two conditions ($\mathrm{Re}_p\mathrm{Sl} = 0.255$ and $\mathrm{Re}_p\mathrm{Sl} = 0.27$), where the escape rate of the perfectly slipping particles is zero during the time interval computed. Again, as $\mathrm{Re}_p\mathrm{Sl}$ increases, this slow escape behavior for the perfect slip case is no longer observed. For example, when $\mathrm{Re}_p\mathrm{Sl} = 0.6$ and $\gamma = 3$, the perfect slip escape rate $\kappa = 0.87$ is larger than the no-slip escape rate $\kappa = 0.33$. We set the upper bound of computations as $\mathrm{Re}_p\mathrm{Sl} = 0.6$ due to the computational cost involved.

The behavior of the escape rate with changing $\mathrm{Re}_p\mathrm{Sl}$ can be understood from the trajectory of individual particles. In Fig. 4, trajectories for the no-slip and perfectly slipping sphere cases

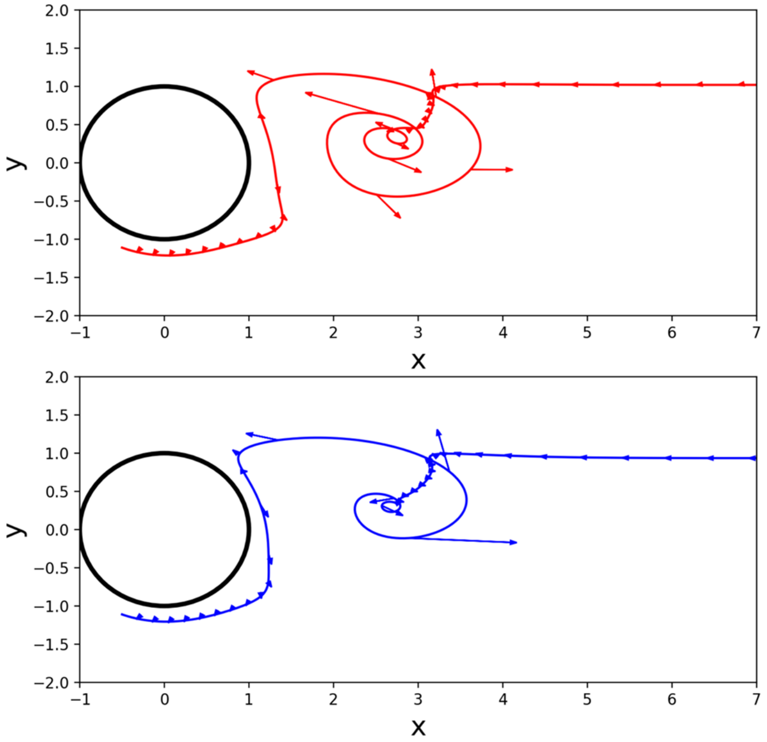

FIG. 5. Comparison of trajectories for a no-slip sphere (top) versus a perfectly slipping sphere (bottom). Initial particle positions are $(-.5, -1.11)$, $\mathrm{Re}_p\mathrm{Sl} = 0.045$, $t_0 = 0$, and $\gamma = 3$. The arrows indicate the direction and magnitude of the history force along a trajectory. Arrow magnitude of no-slip sphere is reduced by one fifth for illustration.

are shown along with the directions of the history force for $\gamma = 0.6$ and $\mathrm{Re}_p\mathrm{Sl} = 0.045$. At these conditions, the history force tends to counteract an outward centrifugal force, thus preventing the particle from escaping. Since the magnitude of the history kernel $[K(t)]$ is larger for a no-slip sphere versus a perfectly slipping sphere $(G(t))$ at fixed t, one might think the no-slip sphere should escape more slowly from the vortex. Indeed, this is case for the conditions in Fig. 4. However, the no-slip sphere does not escape more slowly for all $\mathrm{Re}_p\mathrm{Sl}$. While the perfect slip case may have a smaller magnitude of the history kernel, the history of motion, specifically the particle acceleration, can be drastically different given the same initial position. That is, a perfect slip sphere may have more trajectories that enter the vortex where the no-slip sphere does not. In this case, the perfect slip sphere will enter the vortex and escape downstream at a later time than a no-slip sphere exiting downstream after evading the vortex.

For particles less dense than the surrounding fluid, the history force counteracts the inward centrifugal force of the vortex on the particle. In Fig. 5, trajectories for a no-slip sphere and perfectly slipping sphere with $\gamma = 3$ are shown. The no-slip case history force is much larger than the perfect slip case. Note, for the clarity of illustration, the magnitude of the arrows in the no-slip case in Fig. 5 have been reduced by one-fifth scale than the perfect slip case. Just as for $\gamma = 0.6$, for $\gamma = 3$ whether the escape rate of the no-slip or perfect slip case is larger changes over the range of $\mathrm{Re}_p\mathrm{Sl}$ computed. Again, the no-slip history kernel is larger in magnitude but small differences in the history of motion of the particles can lead to large differences in escape rates. In addition, the two initial conditions in Fig. 5 both result in the no-slip sphere and perfectly slipping sphere being trapped in the vortex; however, the exit y position for the no-slip case is less than zero while the y

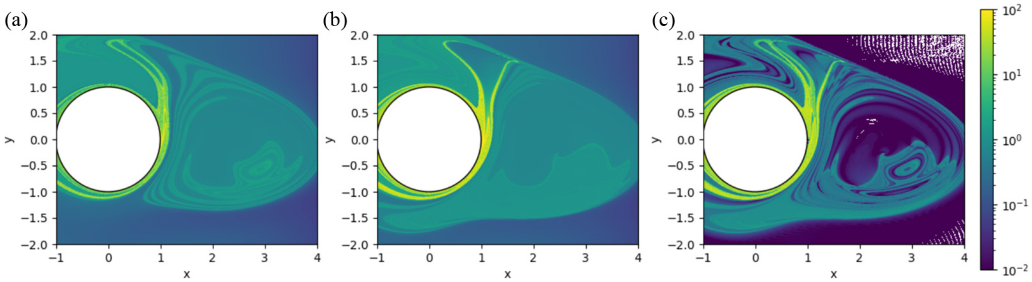

FIG. 6. Residence time distribution of a no-slip sphere (a), a sphere with slip (b), and the absolute difference in residence time between a no-slip sphere and sphere with slip. For this calculation, $\gamma = 3$ and $\mathrm{Re}_p\mathrm{Sl} = 0.09$.

position of the perfectly slipping sphere is approximately 1.5. Given the same initial conditions, there is no guarantee the escape rate or escape position downstream of a no-slip and perfectly slipping sphere will be similar, which is expected given the chaotic nature of trajectories. To capture these differences, we create a residence time distribution for each case next.

B. Residence time distributions

To create a residence time distribution, we calculate the time it takes a particle to escape, for up to 100 periods of vortex shedding, where an escaped particle is defined as a particle that passes the downstream $x = 5$ position. We discard the previous condition excluding trajectories within 0.014 cylinder radii of the cylinder surface to include behavior for long-time escaping particles. The difference in residence time between a no-slip and perfect slip sphere can be $O(100)$ [Fig. 6(c)]. A slipping sphere has significantly more initial conditions that remain in the wake of the cylinder for longer than 100 periods of vortex shedding than the no-slip sphere [Figs. 6(a) and 6(b)]. Qualitatively, this signals that the cylinder surface is stickier in the case of particles with a slipping surface, as particles with long residence times will spend a long time near rear surface of the cylinder. Furthermore, initial conditions of no-slip spheres with long residence times are near the rear stagnation point of the cylinder, while the perfectly slipping case has initial conditions remaining in the cylinder wake for over 100 periods of vortex shedding that begin over one cylinder radius from the cylinder.

This open flow system also exhibits transient chaos, whereby the difference between two trajectories with infinitesimally small perturbations in initial position grows exponentially in time up to a point where particles escape downstream. We now quantify this transient chaos for a no-slip sphere and perfectly slipping sphere. Using the same parameters as in Fig. 6, we identify initial conditions where the particle remains in the wake of the cylinder for longer than 15 vortex periods. These initial conditions trace the stable manifold, or repelling material line, as shown in Fig. 7. This material line is repelling as there is no particle flux through the line and particles initially on opposite sides of this material line are repelled away from each other. Figure 7 shows the evolution of the repelling material lines for no-slip and perfect slip particles at four times after a vortex is shed from the top of the cylinder. This shows that slip can significantly change which initial positions remain for long times in the wake of the cylinder. While both no-slip and slip particles that start near the cylinder surface have large residence times, there are significant differences in the loop formed off the top right of the cylinder in Fig. 8(a). The no-slip material line encloses a smaller area in the loop than the slip case. As time increases, particles trapped in the loop are pulled toward the cylinder surface as they are unable to pass through the repelling material line. Since the area in this loop is smaller for the no-slip case, fewer particles are trapped near the cylinder surface and the escape rate for the slipping sphere is larger than the no-slip sphere at $\mathrm{Re}_p\mathrm{Sl} = 0.09$ as also shown in Fig. 3.

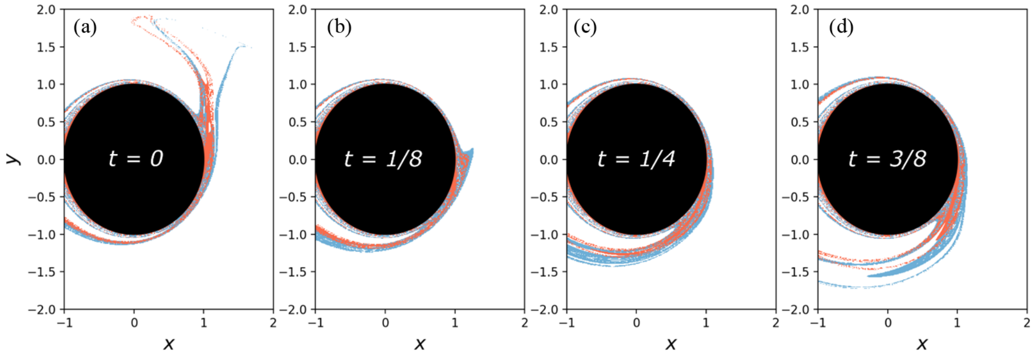

FIG. 7. Stable manifold, or repelling material line, for no-slip spheres are shown in red and perfectly slipping spheres are in blue. Each snapshot of the stable manifold taken as a vortex is shed from the top of the cylinder. For this calculation, $\gamma = 3$ and $\mathrm{Re}_p\mathrm{Sl} = 0.09$.

Central to chaotic systems analysis is the Lyapunov exponent, defined by [25]

$$\delta_t = \delta_0 e^{\lambda t}, \tag{28}$$

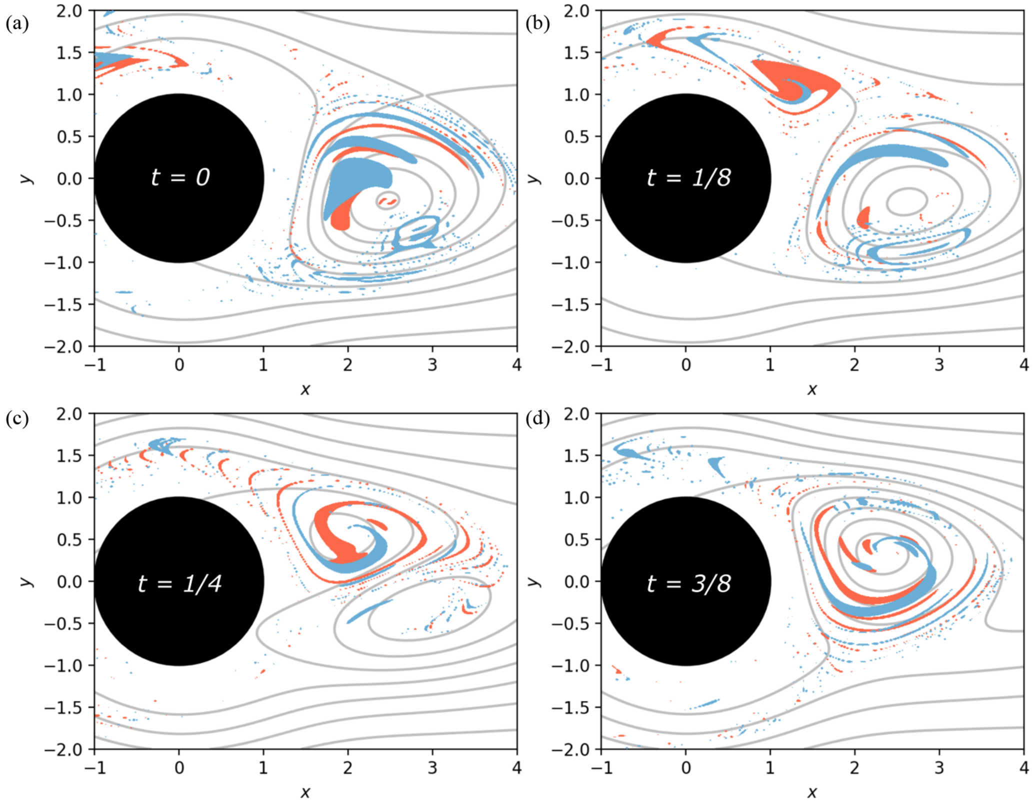

FIG. 8. Unstable manifold, or attracting material line, for no-slip spheres in red and perfectly slipping spheres in blue. The ambient flow streamlines are shown in grey. Each snapshot of the unstable manifold is taken after a vortex is shed from the top of the cylinder. For this calculation, $\gamma = 3$ and $\mathrm{Re}_p\mathrm{Sl} = 0.09$.

where λ is the largest Lyapunov exponent, δ_0 is a small initial distance between two trajectories, and δ_t is the distance between two trajectories at time, t. For chaotic systems $\lambda > 0$ and the distance between the trajectories grows exponentially with larger λ, implying greater separation between the trajectories and therefore a more unstable initial position. However, due to the time-dependent nature of the flow in the wake of a cylinder, a single value for the Lyapunov exponent does not apply to all locations at all times. Instead, we calculate a FTLE field, where regions of high Lyapunov exponent ridges are the unstable manifold, or attracting material line [26]. These regions evolve in space and time due to the unsteady flow. The Lyapunov exponent is calculated at 90 000 grid points for $x = (-1, 4)$ and $y = (-2, 2)$ with the finite time $t = (t_0, t_0 + 10)$ for trajectory computation. Here, we specify the initial time, t_0, as the FTLE field is time dependent. The ridge locations are approximated using a logarithmic scale on a contour plot so only large Lyapunov exponents ($\lambda > 1$) are shown. The unstable manifold is shown in Fig. 8, where the attracting material lines for the no-slip and slip cases are shown after vortex is shed from the top of the cylinder. The material lines for both the no-slip and slip case do not coincide with the fluid streamlines or each other. That is, a no-slip sphere moves along a different trajectory when it enters a vortex than does a slip sphere due to differences in the position of these attracting material lines. This is illustrated in Fig. 5, where both the no-slip and slipping sphere enter the vortex; however, the slipping sphere revolves around the center of the vortex for one period less than the no-slip sphere. Therefore, no-slip and slip spheres will have different trajectories downstream due to the location differences in the attracting material lines.

IV. CHAOTIC SCATTERING

While our previous analysis has focused on the behavior of particles in the wake of the cylinder, we now analyze scattering of particles whose initial position are upstream of the cylinder. Here, we fix the initial position of all trajectories to ($x = -3, y = 0.005$). This is upstream from the cylinder and offset from the x axis to avoid particles sticking to the front of the cylinder. Again, a stuck particle is one that attaches to the surface of the cylinder and does not exit downstream. This particle sticking is due to the JTZ stream-function approximation of the actual fluid flow. We begin by using a method to analyze scattering trajectories developed by Bleher *et al.* [27]. Let our output variable be the residence time, Dt, given by the time it takes for a particle to escape downstream until $x = 5$. Our input variable is the initial time, t_0, for when a particle is released upstream of the cylinder. Results for a no-slip sphere, with $\gamma = 3$, are shown in Fig. 9. In this figure, the residence time increases as we zoom in on singular regions of residence time versus initial time plot. Two types of trajectories occur: regular path lines and scattering path lines. Regular path lines are particles deflected by the cylinder and exit downstream without entering the vortex behind the cylinder. Regular path lines have lower residence times and regions in Fig. 9 that are smooth contain these path lines. Scattering path lines are path lines where the particle follows close to the cylinder surface before passing through the rear stagnation point of the cylinder. These particles remain trapped near the rear of the cylinder for long times. Regions in Fig. 9 with large variances in residence time for small changes in t_0 are evidence of chaotic scattering path lines. For the no-slip case, the residence time increases significantly from Figs. 9(a) to 9(b) due to singularities in the residence time being magnified, which appear due to particles being trapped at the rear stagnation point of the cylinder [19]. As we approach these singularities, the residence times increase as the particle gets closer and closer to the rear stagnation point of the cylinder. While scattering trajectories typically deviate from a baseline residence time of regular particle trajectories, in Fig. 9(b), this baseline itself seems to increase for initial times around 0.045. This is due to the path line approaching very close to the upstream cylinder surface, thereby increasing the time to reach the wake of the cylinder, i.e., this is not due to chaotic scattering in the wake.

We complete the same analysis for the perfect slip case with $\gamma = 3$, shown in Fig. 10. Again, we see regular path-line sections and scattering path-line sections as in the no-slip case. However, the residence time is larger in the perfect slip case, as evidenced by having many more initial times

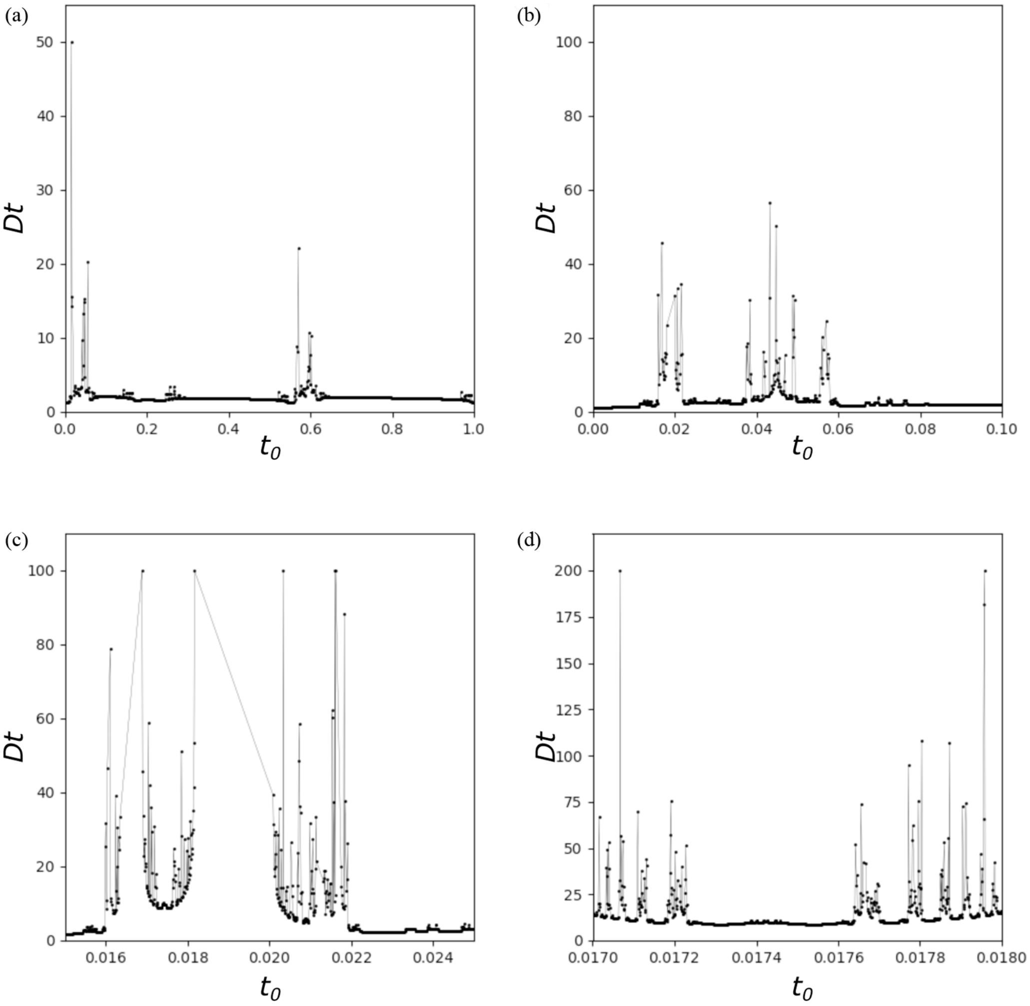

FIG. 9. No-slip sphere residence time, Dt, versus the initial time, t_0, that a particle is released over a period of vortex shedding in plot (a). Subsequent plots (b)–(d) show small scale variance in residence time as the interval of initial time shrinks, which indicates chaotic scattering.

leading to residence times larger than 200 vortex periods. In addition, Fig. 10(d) shows significant variation for initial times differing by only 10^{-6}. To quantify this difference, we estimate the uncertainty dimension using a method adapted from Refs. [27,28]. Here, we have selected a domain of initial times, $t_0 = 0$ to $t_0 = 0.1$ since scattering seems to occur soon after a vortex is shed from the cylinder surface, either at $t_0 = 0$ (shed from top) or $t_0 = 0.5$ (shed from bottom) [see Fig. 10(a)]. Next, we estimate an uncertainty probability, $f(\epsilon)$, by computing a trajectory started at t_0 and a trajectory perturbed an amount ϵ in time, i.e., started at $t_0 + \epsilon$. If the trajectories remain on the same side of the x axis, they are not uncertain. If the trajectories end up on opposite sides of the x axis, they are uncertain. This is computed for $N = 10\,000$ randomly selected trajectories and the uncertainty probability is $f(\epsilon) = N_0/N$, where N_0 is the number of uncertain trajectory pairs. For small ϵ, the scaling of the uncertainty probability is $f(\epsilon) = \epsilon^{\alpha}$, and the uncertainty dimension $D_s = 3 - \alpha$ for this three-dimensional system (two spatial dimensions and one dimension in time). Figure 11 shows the uncertainty probability for both a no-slip and perfect slip sphere over a range of ϵ. The uncertainty dimension for a no-slip sphere is 2.74 while the uncertainty dimension for the perfect

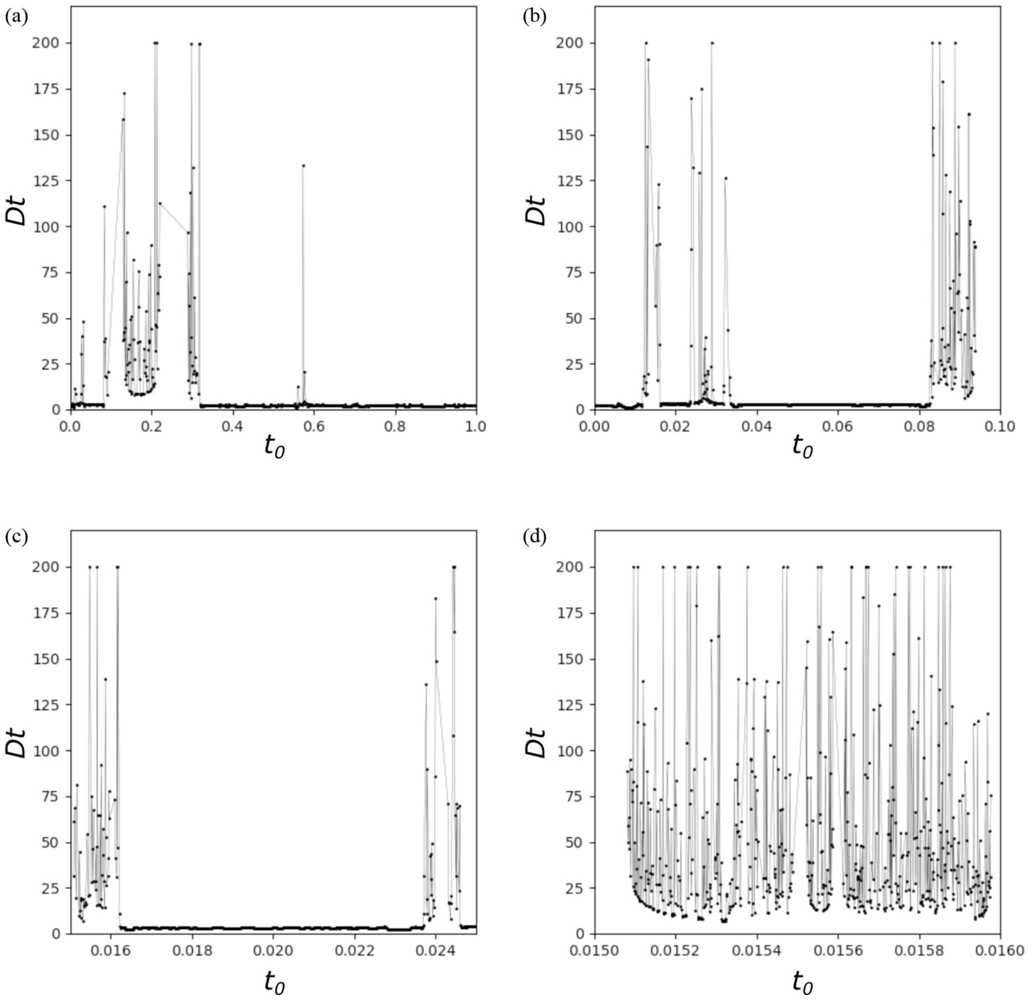

FIG. 10. Slipping sphere residence time, Dt, versus initial time, t_0, over one period of vortex shedding in plot (a). Subsequent plots (b)–(d) show small scale variance in residence time as interval of initial time shrinks.

slip sphere is 2.84. This indicates a higher degree of uncertainty for the perfect slip case. Figure 11 can also be interpreted by viewing the x axis as a measurement error and the y axis as the fraction of instances a prediction is incorrect due to this error. As expected, as the measurement error decreases, predictions become more accurate. This is seen by $f(\epsilon)$ decreasing with decreasing ϵ. However, the rate at which $f(\epsilon)$ decreases indicates the uncertainty of the system. So, the uncertainty dimension for the perfect slip sphere is larger than the no-slip sphere since the slope of the perfect slip line in Fig. 11 is smaller than that of the no-slip line. That is, as our measurement error decreases, our prediction accuracy improves less in the perfect slip case than the no-slip case.

V. CONCLUSION

Calculations for the motion of small spherical particles, with and without surface hydrodynamic slip, in unsteady 2D von Kármán flow at the wake of a circular cylinder flow were performed. For $\mathrm{Re}_p\mathrm{Sl} < 1$, the escape rate of a perfectly slipping sphere can be 50% larger than the no-slip sphere for particles more dense than the surrounding fluid. Residence time distributions for initial

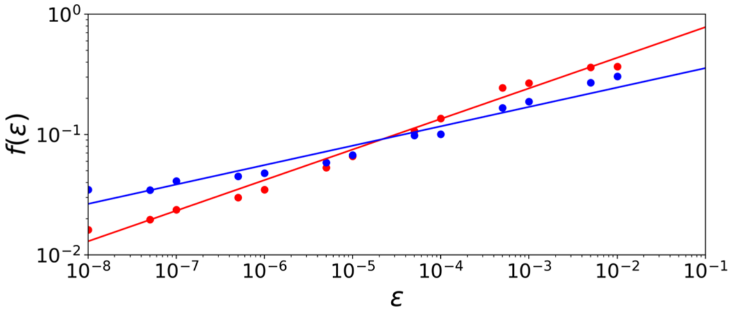

FIG. 11. Log-log plot of uncertainty probability versus perturbation (ϵ) for no-slip (red line of best fit and red dots) and perfectly slipping sphere (blue line of best fit and blue dots).

conditions in the wake of the cylinder also show qualitative differences of which initial conditions lead to long time trajectories in each case. The perfectly slipping sphere has significantly more initial conditions that remain in the wake of the cylinder for longer than 15 vortex shedding periods. This is also evident in the stable manifold and unstable manifold, which qualitatively differ in location for no-slip and slip cases.

Chaotic scattering of no-slip and perfect slip spheres was analyzed by computing the residence time of a particle initially upstream of the cylinder for many different initial times. Both the no-slip and perfect slip spheres show large variations in residence time for small changes in initial time, and thus both show evidence of chaotic scattering. The uncertainty dimension is calculated to provide a quantitative measure of uncertainty given a measurement error. Here, the perfect slip sphere has a higher uncertainty dimension than the no-slip sphere, indicating prediction accuracy increasing less for the perfect slip sphere as measurement accuracy increases.

While most work on particle motion in unsteady flows has assumed rigid no-slip spheres, we have shown that a change in hydrodynamic surface condition can lead to large differences in the motion of both individual particles (downstream exit positions, trajectories, and scattering behavior) and ensemble behavior (escape rates, material line locations, and residence time distributions). This is relevant for many instances beyond the perfectly slipping particle that we have considered, including bubbles, drops, and slipping spheres with a finite slip length.

Here, we analyzed the two limiting cases (no-slip and perfect slip, i.e., an infinite slip length) of the surface boundary condition on a particle. However, other particles could have finite slip at the particle surface or, as in the case of drops, have mobile fluid-fluid interfaces. In the finite slip length case, the memory kernel is of the same functional form as the perfect slip case but includes factors that are a function of the magnitude of the slip length. Legendre *et al.* [29] numerically calculated an approximation of the history force for a drop. For all viscosity ratios of drop viscosity to fluid viscosity, the kernel is integrably singular as $t \to t_0$ so numerical methods need to be developed similar to that of Daitche [23]. Our analysis also has been for the model problem of an open chaotic flow in the wake of the cylinder. There are other flow systems already analyzed for the no-slip case that could be used to compare to the drop and (finite or perfect) slip cases. For example, Candelier *et al.* [30] analyze, using experiments and theory, the rigid body rotation behavior of no-slip particles dropped into a rotating cylindrical tank filled with a fluid. They show that the no-slip history force is important in prediction of the rate at which a particle, more dense than the surrounding fluid, is ejected from the center of the flow for a particle. This sensitive dependence on history force could lead to differences in ejection behavior given differences in hydrodynamic surface condition.

Finally, we revisit our assumption that the flow at the particle-scale obeys the unsteady Stokes equations, which requires $\mathrm{Re}_s = (a^2 s/\nu) \ll 1$, $\mathrm{Re}_p = aW/\nu \ll 1$, and $\mathrm{Re}_p\mathrm{Sl} = (a^2/\tau\nu) = O(1)$. Specifically, the unsteadiness time scale τ for the JTZ flow is on the order of the time period of vortex shedding from the rear of the cylinder. This timescale is of order L/U, as discussed by Ref. [19]. Hence, $\mathrm{Re}_s \sim \mathrm{Re}_p\mathrm{Sl}$, which implies that inertial lift forces would be comparable to the history force on a particle in this flow. Thus, our assumption of an unsteady Stokes flow at the particle scale is questionable. However, this same assumption was made in Refs. [8,24] to compute the trajectory of a no-slip sphere in the JTZ flow. Thus, the comparison of our results for perfect-slip spheres to that of Refs. [8,24] for no-slip spheres is consistent, since those studies also neglect inertial lift. This comparison serves to demonstrate that hydrodynamic slip significantly alters chaotic advection and scattering of small particles, due to the difference in the history force between the perfect-slip and no-slip cases, which is the main conclusion of our paper.

Extending our computations to include the effects of inertial lift would be very challenging. Technically, it would require that Eqs. (1) and (5) for the hydrodynamic force on a no-slip and perfect-slip sphere, respectively, be augmented with appropriate expressions for the inertial force (lift and drag) due to the local velocity gradient in the flow. Such expressions would first have to take into account the time-dependence of the relative velocity, $\boldsymbol{v} - \boldsymbol{u}$, between the particle and fluid. (Note, this relative velocity is termed a slip velocity in the literature on inertial lift, but this is not to be confused with the hydrodynamic slip that we consider.) Second, the time-dependence in the local velocity gradient must be accounted for. That is, we require an expression for the inertial force on a spherical particle with a time-dependent slip velocity in a time-dependent velocity gradient at $\mathrm{Re}_s \ll 1$ and $\mathrm{Re}_p \ll 1$. To our knowledge, such an expression does not exist. Indeed, an expression for the time-dependent inertial force on a (no-slip) particle with a time-dependent slip velocity in a steady velocity gradient was only recently derived in Ref. [31], under the restrictions that $\mathrm{Re}_s \ll 1$, $\mathrm{Re}_p \ll 1$, $\sqrt{\mathrm{Re}_s}/\mathrm{Re}_p \ll 1$, and $\mathrm{Sl}\mathrm{Re}_s \ll 1$. The first three restrictions are the same as imposed by Saffman [32] in his seminal work on the steady inertial lift force on a sphere steadily translating along the streamlines of steady simple shear flow. The last restriction means unsteady and convective inertial effects matter only at large distances, of order $1/\sqrt{\mathrm{Re}_s}$, from the particle. We view the consideration of how inertial lift forces affect the particle trajectories that we have presented to be an important direction for future work.

ACKNOWLEDGMENTS

J.K.K. thanks the Sharbaugh Presidential Fellowship and Dighe Fellowship for financial support.

[1] G. Falkovich, A. Fouxon, and M. G. Stepanov, Acceleration of rain initiation by cloud turbulence, Nature (London) **419**, 151 (2002).

[2] S. Olivieri, F. Picano, G. Sardina, D. Ludicone, and L. Brandt, The effect of the basset history force on particle clustering in homogeneous and isotropic turbulence, Phys. Fluids **26**, 041704 (2014).

[3] A. Daitche, On the role of the history force for inertial particles in turbulence, J. Fluid Mech. **782**, 567 (2015).

[4] R. Toegel, S. Luther, and D. Lohse, Viscosity Destabilizes Sonoluminescing Bubbles, Phys. Rev. Lett. **96**, 114301 (2006).

[5] S. Wang and A. M. Ardekani, Unsteady swimming of small organisms, J. Fluid Mech. **702**, 286 (2012).

[6] J. Hubbard, J. Haglund, and O. Ezekoye, Simulation of the evolution of particle size distributions containing coarse particulate in the atmospheric surface layer with a simple convection-diffusion-sedimentation model, Atmos. Environ. **43**, 4435 (2009).

[7] M. R. Maxey and J. J. Riley, Equation of motion for a small rigid sphere in a nonuniform flow, Phys. Fluids **26**, 883 (1983).

[8] A. Daitche and T. Tél, Memory Effects are Relevant for Chaotic Advection of Inertial Particles, Phys. Rev. Lett. **107**, 244501 (2011).

[9] A. Basset, *A Treatise on Hydrodynamics* (Deighton, Bell and Co., Cambridge, UK, 1888), Vol. 2.

[10] V. A. Gorodtsov, Slow motions of a liquid drop in a viscous liquid, J. Appl. Mech. Tech. Phys. **16**, 865 (1976).

[11] S. Yang and L. G. Leal, A note on memory-integral contributions to the force on an accelerating spherical drop at low Reynolds number, Phys. Fluids **3**, 1822 (1991).

[12] B. J. Alder and T. E. Wainwright, Decay of the velocity autocorrelation function, Phys. Rev. A **1**, 18 (1970).

[13] A. R. Premlata and H.-H. Wei, The Basset problem with dynamic slip: Slip-induced memory effect and slip-stick transition, J. Fluid Mech. **866**, 431 (2019).

[14] J. K. Kabarowski and A. S. Khair, Unsteady motion of a perfectly slipping sphere, Phys. Rev. E **101**, 053102 (2020).

[15] J. Mo, A. Simha, and M. G. Raizen, Brownian motion as a new probe of wettability, J. Chem. Phys. **146**, 134707 (2017).

[16] V. Galindo and G. Gerbeth, A note on the force on an accelerating spherical drop at low-Reynolds number, Phys. Fluids **5**, 3290 (1993).

[17] H. Aref, Stirring by chaotic advection, J. Fluid Mech. **143**, 1 (1984).

[18] R. Liu, M. Stremler, K. Sharp, M. Olsen, J. Santiago, R. Adrian, H. Aref, and D. Beebe, Passive mixing in a three-dimensional serpentine microchannel, J. Microelectromech. Syst. **9**, 190 (2000).

[19] C. Jung, T. Tél, and E. Ziemniak, Application of scattering chaos to particle transport in a hydrodynamical flow, Chaos **3**, 555 (1993).

[20] M. R. Maxey, The equation of motion for a small rigid sphere in a nonuniform or unsteady flow, in *Proceedings of Gas-Solid Flows*, The Fluids Engineering Conference, Washington, D.C. (1994), Vol. 166.

[21] E. E. Michaelides and Z.-G. Feng, The equation of motion of a small viscous sphere in and unsteady flow with interface slip, Int. J. Multiphase Flow **21**, 315 (1995).

[22] J. C. Sommerer, H.-C. Ku, and H. E. Gilreath, Experimental Evidence for Chaotic Scattering in a Fluid Wake, Phys. Rev. Lett. **77**, 5055 (1996).

[23] A. Daitche, Advection of inertial particles in the presence of the history force: Higher order numerical schemes, J. Comput. Phys. **254**, 93 (2013).

[24] A. Daitche and T. Tél, Memory effects in chaotic advection of inertial particles, New J. Phys. **16**, 073008 (2014).

[25] S. H. Strogatz, *Nonlinear Dynamics and Chaos with Student Solutions Manual: With Applications to Physics, Biology, Chemistry, and Engineering* (CRC Press, Boca Raton, FL, 2018).

[26] S. C. Shadden, F. Lekien, and J. E. Marsden, Definition and properties of Lagrangian coherent structures from finite-time Lyapunov exponents in two-dimensional aperiodic flows, Physica D **212**, 271 (2005).

[27] S. Bleher, E. Ott, and C. Grebogi, Routes to Chaotic Scattering, Phys. Rev. Lett. **63**, 919 (1989).

[28] M. Raj Banerjee and G. Subramanian, An anisotropic particle in a simple shear flow: An instance of chaotic scattering, J. Fluid Mech. **913**, A2 (2021).

[29] D. Legendre, A. Rachih, C. Souilliez, S. Charton, and E. Climent, Basset-Boussinesq history force of a fluid sphere, Phys. Rev. Fluids **4**, 073603 (2019).

[30] F. Candelier, J. R. Angilella, and M. Souhar, On the effect of the Boussinesq-Basset force on the radial migration of a Stokes particle in a vortex, Phys. Fluids **16**, 1765 (2004).

[31] F. Candelier, B. Mehlig, and J. Magnaudet, Time-dependent lift and drag on a rigid body in a viscous steady linear flow, J. Fluid Mech. **864**, 554 (2019).

[32] P. G. Saffman, The lift on a small sphere in a slow shear flow, J. Fluid Mech. **22**, 385 (1965).